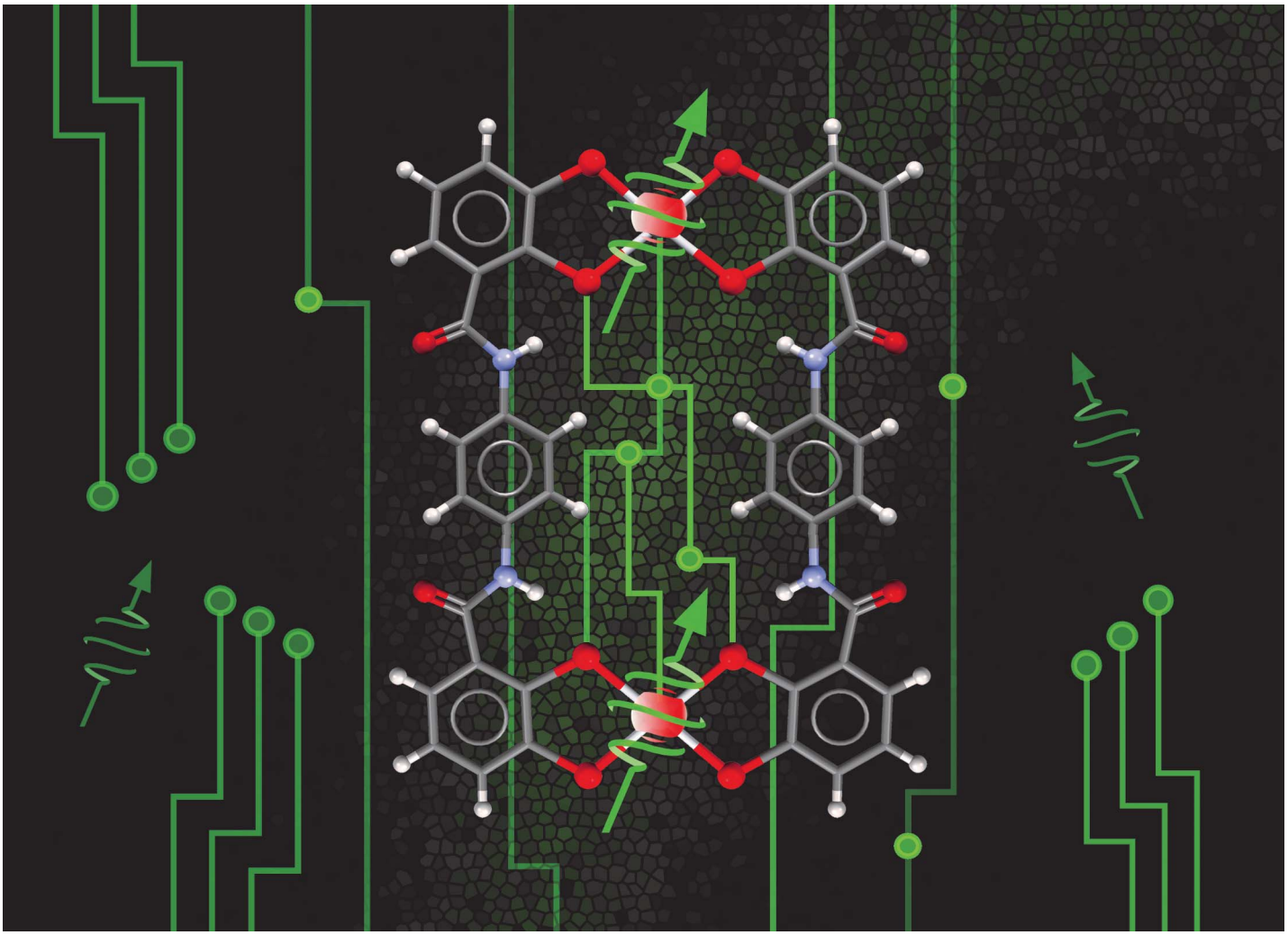

Showcasing research from Professor Roberta Sessoli's laboratory, Department of Chemistry, University of Florence, Italy, and Professor Stefano Carretta's research group, Department of Mathematics, Physics and Informatics, University of Parma, Italy.

A two-qubit molecular architecture for electron-mediated nuclear quantum simulation

A molecular architecture where two weakly interacting vanadyl-based qubits are linked together is described and investigated here as a platform for quantum simulation. Fast electronic spin excitations are used to switch the effective interaction between qubits encoded in vanadium(IV) nuclear spin states. The experimentally derived spin Hamiltonian parameters of the system, which shows remarkably long electronic coherence times, have been used to simulate the system dynamics under specific sequence of pulses. This demonstrates the possibility of using this molecular complex to implement a control-Z gate and simple quantum simulations.

As featured in:

See Matteo Atzori, Stefano Carretta, Roberta Sessoli *et al.*, *Chem. Sci.*, 2018, **9**, 6183.

ROYAL SOCIETY OF CHEMISTRY

rsc.li/chemical-science

Registered charity number: 207890

Chemical Science

EDGE ARTICLE

View Article Online
View Journal | View Issue

Cite this: *Chem. Sci.*, 2018, **9**, 6183

A two-qubit molecular architecture for electron-mediated nuclear quantum simulation†

Matteo Atzori, *[a] Alessandro Chiesa, [bc] Elena Morra, [d] Mario Chiesa, [d] Lorenzo Sorace, [a] Stefano Carretta *[b] and Roberta Sessoli *[a]

A switchable interaction between pairs of highly coherent qubits is a crucial ingredient for the physical realization of quantum information processing. One promising route to enable quantum logic operations involves the use of nuclear spins as protected elementary units of information, qubits. Here we propose a simple way to use fast electronic spin excitations to switch the effective interaction between nuclear spin qubits and the realization of a two-qubit molecular architecture based on highly coherent vanadyl moieties to implement quantum logic operations. Controlled generation of entanglement between qubits is possible here through chemically tuned magnetic coupling between electronic spins, which is clearly evidenced by the splitting of the vanadium(IV) hyperfine lines in the continuous-wave electron paramagnetic resonance spectrum. The system has been further characterized by pulsed electron paramagnetic resonance spectroscopy, evidencing remarkably long coherence times. The experimentally derived spin Hamiltonian parameters have been used to simulate the system dynamics under the sequence of pulses required to implement quantum gates in a realistic description that includes also the harmful effect of decoherence. This demonstrates the possibility of using this molecular complex to implement a control-Z (CZ) gate and simple quantum simulations. Indeed, we also propose a proof-of-principle experiment based on the simulation of the quantum tunneling of the magnetization in a $S = 1$ spin system.

Received 13th April 2018
Accepted 13th June 2018

DOI: 10.1039/c8sc01695j

rsc.li/chemical-science

Introduction

Quantum Information Processing (QIP) has the promise to shift the current computational paradigm based on classical bits to a more performing computational protocol that exploits the quantum properties of matter to perform quantum logic operations, *i.e.* quantum gates.[1] The physical realization of quantum computers[2,3] can be in principle achieved by using a variety of quantum systems, such as superconducting circuits,[4] photons,[5–7] or electronic defects in inorganic solids.[8,9]

Molecular spin qubits have recently emerged as an alternative platform with great promise in terms of long coherence times and fine-tuning of their magnetic/electronic properties.[10–17] The current challenge is the realization of molecular quantum gates based on two or more interacting qubits with a long coherence time that can be efficiently manipulated by electromagnetic radiation pulses. Supramolecular assemblies of heterometallic Cr_7Ni rings[18–21] and dinuclear lanthanide complexes[22,23] are currently the most investigated systems for this purpose. Although they represent elegant realizations of coupled molecular qubits, further improvements such as narrow Electron Paramagnetic Resonance (EPR) spectral lines are necessary to allow precise qubit control. Also, long coherence times retained at high temperatures would be important for practical applications.

These features have been partially achieved through a fine engineering of the Landé g factor in organic multiradical systems to address different qubits individually.[24,25] However, they present permanent qubit–qubit interactions that lead to an unwanted continuous many body evolution that has to be corrected during gating through complex pulse sequences.

An alternative possibility to the use of electronic spins is the use of nuclear spins to encode qubits that are more weakly coupled to the environment and hence substantially protected from decoherence.[26] Indeed, Grover's quantum search algorithm has been recently implemented on a multilevel system consisting of a Tb^{III} nuclear spin sitting on

[a]Dipartimento di Chimica "Ugo Schiff" & INSTM, Università Degli Studi di Firenze, I-50019 Sesto Fiorentino, Italy. E-mail: matteo.atzori@unifi.it; roberta.sessoli@unifi.it

[b]Dipartimento di Scienze Matematiche, Fisiche e Informatiche, Università di Parma, I-43124 Parma, Italy. E-mail: stefano.carretta@unipr.it

[c]Institute for Advanced Simulation, Forschungszentrum Jülich, D-52425 Jülich, Germany

[d]Dipartimento di Chimica & NIS Centre, Università di Torino, Via P. Giuria 7, I-10125 Torino, Italy

† Electronic supplementary information (ESI) available: Additional figures, tables, equations and computational details as mentioned in the text. See DOI: 10.1039/c8sc01695j

a molecular transistor and controlled by electric fields.[27,28] However, purely nuclear spin platforms have the drawback of showing very weak and permanent direct couplings, yielding very slow two-qubit gates and unwanted two-qubit evolutions.[26]

Hybrid electron-nuclear approaches,[8,29–33] exploiting electronic transitions to achieve a universal control of nuclear qubits *via* sophisticated sequences of pulses, have been proposed.[24,34–38] In particular, electrons allow one to obtain high nuclear polarization, thus enabling the initialization of the nuclear register,[37] while nuclei provide long coherence times, as shown in Electron-Nuclear Double Resonance (ENDOR) based QIP.[31]

Here we propose a novel scheme for electron-mediated nuclear quantum simulation. In contrast to recently reported NMR quantum computation approaches,[25] we do not rely on the free evolution induced by the internal Hamiltonian to drive two-qubit gates. Furthermore, the qubit–qubit coupling is not permanent. Indeed, in our approach the interaction between nuclear qubits is effectively and rapidly switched on and off by exciting the coupled electronic spins *via* simple microwave (EPR-like) pulses, while single-qubit rotations between decoupled nuclear spins are obtained by means of radio-frequency (NMR-like) pulses. This leads to simple pulse sequences, thus requiring few operations, for the implementation of quantum simulations. In addition, individual spin addressing and the related ***g***-engineering are not needed to simulate symmetric quantum mechanical problems.

A prototypical realization of this idea is a molecular architecture composed of two paramagnetic metal ions with magnetic nuclei ($I \neq 0$) and sizeable hyperfine couplings. Indeed, a small but measurable interaction between the two electronic spins can be used to effectively couple nuclear qubits and controllably generate entangled two-qubit states. Long electronic spin coherence times are also a key ingredient to ensure the robustness of such a system during the implementation of electron-mediated two-qubit gates.

To this aim, we have synthesised a dinuclear molecular architecture consisting of two weakly interacting vanadyl moieties. They are the ideal building blocks for this scheme thanks to their magnetic nuclei ($I = 7/2$), large hyperfine splitting, and long coherence times.[15] We have fully characterized the system by continuous-wave and pulsed EPR measurements, thus extracting all the parameters of the spin Hamiltonian, as well as the phase memory time. This was found to be remarkably long (*ca.* 1 μs) and of the same order of magnitude as that of a representative mononuclear derivative.[39] We have used the set of parameters determined from EPR spectroscopy to numerically simulate the dynamics of the system subject to the microwave (mw) and radio-frequency (rf) pulses necessary to implement single and two-qubit gates. Our realistic simulations also include the detrimental effect of decoherence in a Lindblad master-equation formalism.[40] Finally, we have designed a proof-of-principle experiment of quantum simulation that could be implemented with the present system.

Results and discussion

Electron-mediated nuclear-spin QIP: conception, design and synthesis

A sketch of the proposed scheme is shown in Fig. 1. It consists of a dinuclear molecular architecture of transition metal ions with both electronic ($s_{1,2}$) and nuclear spins ($I_{1,2}$). The electronic spins are coupled by an interaction (described by J) and each nuclear spin is coupled to its electronic spin *via* the hyperfine interaction (described by **A**).

In significant magnetic fields, the electronic and nuclear spin states are practically factorized because of the large difference in their Zeeman energies. Hence, if electrons stay in their ground state, the effect of the hyperfine interaction $\left(H_{\mathrm{hyp}} = \sum_{i=1,2} \boldsymbol{I}_i \cdot \boldsymbol{A} \cdot \boldsymbol{s}_i\right)$ is simply equivalent to a renormalization of the magnetic field felt by the nuclear spins. Therefore, the energy to rotate one of the nuclear spins does not depend on the state of the other. By using a pair of nuclear spin states to encode the qubits, single-qubit rotations can then be implemented by means of rf pulses resonant with the nuclear Zeeman energy gap. Conversely, the energy to rotate the coupled electron spins depends on the state of both nuclei, because of the hyperfine coupling. Thus, the effect of a resonant mw pulse depends on the states of the nuclear qubits and this can be directly exploited to implement a conditional two-qubit gate. Hence, the two coupled electron spins act as a sort of fast switch of the effective interaction between nuclear qubits.

Potential building blocks for a molecular realization of such a two-qubit architecture are coordination compounds of vanadium(IV) ions. Indeed, recent promising results in terms of long coherence times related to a manifold of narrow resonance lines have been reported for a variety of vanadium(IV) molecular single-qubit systems,[12–16] in particular those where the vanadium(IV) is embedded in a vanadyl moiety.[12–15] Several efforts have been devoted to establishing chemical design strategies to increase both the coherence time T_m[12,41] and the spin-lattice relaxation time T_1,[12,39] but the realization of a molecular system containing two weakly interacting single *d*-metal ions for the purpose of quantum gate implementation is still missing.

To address this challenge, we have selected ditopic-catecholate ligands as suitable qubit-linking systems. These ligands allow the modulation of the qubit–qubit distance by changing the central spacer, providing a fine-tuning of the magnetic interaction (Fig. 2). Moreover, catecholates have been recently identified as ideal ligands to prepare single-qubit

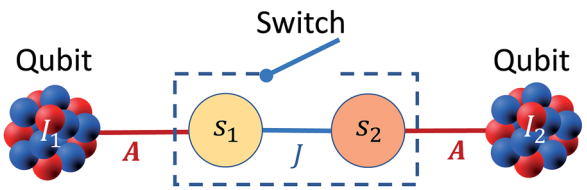

Fig. 1 Sketch of the proposed hybrid nuclear-electronic architecture for QIP.

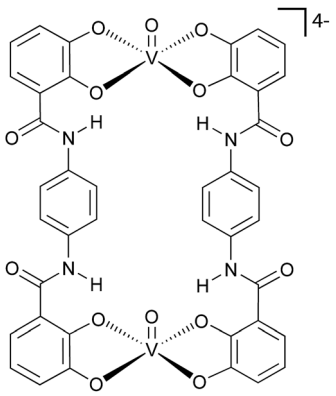

Fig. 2 Molecular structure of the vanadyl-based two-qubit molecular architecture (**1**).

vanadium(IV)-complexes with long spin-lattice relaxation and long spin coherence times.[39] By following this approach, we targeted and succeeded in the preparation of a molecular system of the formula $[PPh_4]_4[(VO)_2(L_1)_2]$ (**1**) (L_1 = tetraanion of $C_6H_3(OH)_2$–CONH–C_6H_4–CONH–$C_6H_3(OH)_2$) (Fig. 2), which can be used to implement our QIP scheme. The properties of **1** are herein compared to that of a recently reported mononuclear compound of the formula $[PPh_4]_2$[VO(catecholate)$_2$] (**2**)[39] that has been taken as a reference.

Compound **1** shows low solubility in most of the common organic solvents, being soluble only in the most polar ones such as dimethylformamide (DMF) and dimethylsulfoxide (DMSO). This precluded a crystallographic analysis through single crystal X-ray diffraction. To provide structural insights into the molecular structure of **1** we have supported the classical analytical characterization (see the Experimental section) with hyperfine sublevel correlation (HYSCORE) spectroscopy experiments at the Q-band frequency. HYSCORE data for **1** show a diagonal peak at the ^{51}V Larmor frequency (Fig. S1†). From the presence of a diagonal peak, a lower limit of 5 Å for the V···V distance can be estimated based on a pure dipole–dipole interaction. This diagonal peak is not observed for monomeric vanadyl complexes at comparable concentrations, strongly supporting the existence of a dinuclear structure with a well-defined V···V distance compatible with the ligands used.[42,43] Cross peaks due to the hyperfine coupling with a ^{14}N ($I = 1$) nucleus (*ca.* 4.5 MHz) are also observed when dissolving the complex in DMF but not in DMSO (Fig. S1†). This excludes an interaction originating from the amidic nitrogen atom of the ligand and suggests the presence of an interaction with a DMF solvent molecule in the equatorial plane, as already reported for other vanadyl complexes.[44,45] The comparison of the X-band EPR spectra of **1** recorded in DMF and DMSO, which are completely superimposable (Fig. S2†), confirms that interaction with the solvent does not significantly affect the molecular structure in solution.

Magnetic characterization and spectroscopic studies by CW- and pulsed-EPR

The V^{IV} spin centres in compound **1** are not directly connected through a bridging ligand. Therefore, the most relevant magnetic interaction is expected to be through-space, that is, a dipolar interaction. On the basis of the estimated V···V distance, this should be of the order of 3×10^{-3} cm^{-1} and accordingly its magnetic behaviour follows a Curie–Weiss law (Fig. S3†).

Frozen solution continuous wave EPR spectra of **1** were recorded to get insights into its electronic properties and to determine with reasonable accuracy the magnitude of the dipolar qubit–qubit interaction. The spectrum shows an eight-fold hyperfine splitting due to the coupling between the $s = 1/2$ electronic spin of V^{IV} and the $I = 7/2$ nuclear spin of ^{51}V (natural abundance 99.76%). The signal is further split by the anisotropic components of the Landé factor and the hyperfine coupling. Furthermore, each hyperfine resonance line appears additionally split into two components (Fig. 3a), a phenomenon which can be attributed to the weak dipolar coupling between the V^{IV} spins. Importantly, such a splitting is not observed in the spectrum of the reference compound **2**.[39]

Spectral simulations[46] were performed on the basis of the following spin Hamiltonian‡ (for an easier discussion of

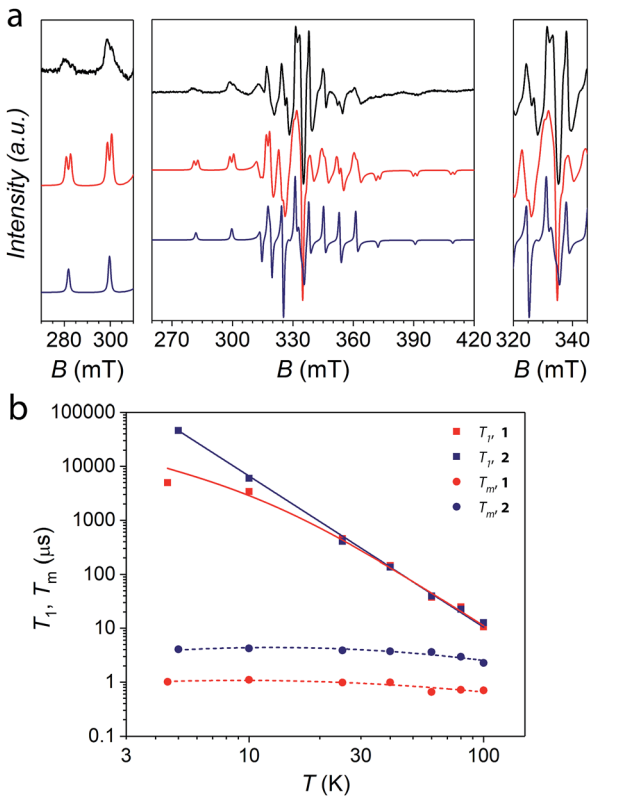

Fig. 3 (a) Experimental frozen solution (0.75 mM in DMF) spectrum of **1** at $T = 10$ K and the X-band frequency (9.39 GHz) (black line). Spectral simulation assuming a dipolar magnetic interaction (red line) and comparison with the non-interacting case (blue line). Lateral panels are zooms over the regions of allowed parallel and perpendicular transitions from states characterized by $|m_{I1}, m_{I2}\rangle = |7/2, 7/2\rangle$ and $|5/2, 5/2\rangle$. They are the relevant ones for our computational basis. (b) Temperature dependence of T_1 and T_m for **1** and **2** at the X-band frequency in a frozen solution of DMSO and DMF, respectively. Solid lines are the best-fit of the model (see the ESI†). Dashed lines represent a guide for the eyes. Error bars are within the size of the symbols.

quantum gates, *vide infra*, z has been chosen along the V···V direction and y as the principal axis of the single spin $\boldsymbol{g}$ and $\boldsymbol{A}$ anisotropy, *i.e.* along the V=O bond):

$$H = \sum_{i=1,2} \boldsymbol{I}_i \cdot \boldsymbol{A} \cdot \boldsymbol{s}_i + \mu_B \sum_{i=1,2} \boldsymbol{s}_i \cdot \boldsymbol{g} \cdot \boldsymbol{B} + J\left(2s_{z1}s_{z2} - s_{x1}s_{x2} - s_{y1}s_{y2}\right) \quad (1)$$

This allowed us to satisfactorily simulate the spectrum of **1** at both X-(Fig. 3a) and Q-band (Fig. S4†) frequencies by considering the two V^{IV} ions as axially symmetric and equivalent and using the following parameters: $g_z = 1.982 \pm 0.002$, $g_x = 1.982 \pm 0.002$, $g_y = 1.941 \pm 0.001$, $A_z = 186 \pm 2$ MHz, $A_x = 186 \pm 2$ MHz, $A_y = 498 \pm 4$ MHz, and $J = -(1.65 \pm 0.10) \times 10^{-3}$ cm^{-1}. This gives the energy pattern reported in Fig. S5†, where the two $M_S = 0$ states are largely overlapping. The principal values of Zeeman and hyperfine tensors are in the expected range for vanadyl paramagnetic centers.[12–14] The value of the spin–spin interaction is consistent with a purely dipolar interaction for an interatomic V···V distance of 10.1 ± 0.2 Å, which is in agreement with expectations based on HYSCORE results and ligand connectivity. We also note that the through-space isotropic contribution arising from the anisotropy of the $\boldsymbol{g}$ tensors is calculated to be negligible and has no effect on the simulated spectrum.

Inversion recovery and echo decay experiments were performed at the X-band frequency to investigate the temperature dependence (4.5–100 K T range) of the spin-lattice relaxation time T_1, and the coherence time T_m, respectively. The extracted values of T_1 and T_m obtained from the fit of the inversion recovery and echo decay traces (Fig. S6†) are reported in Fig. 3b. T_1 and T_m values for the single-qubit reference compound **2** are also reported for comparison. The coherence times of the order of 1 μs are detected for **1** up to 100 K. Although these values are reduced by a factor of *ca.* 4 with respect to the reference single-qubit system **2**, they are comparable or slightly higher than those reported for molecular dimers based on either Cr_7Ni rings[21] or lanthanide complexes.[23] The coherence time decrease from 4 μs to 1 μs in the two-qubit quantum gate **1** is not surprising given the presence of a proximal vanadium(IV) electronic magnetic moment and the nuclear-spin active (^{1}H and ^{14}N) richer molecular structure needed to link two spin centres. We note that observing such long coherence times for two electronic spins placed in close proximity is not commonplace. This result indicates that the molecular design of the qubits (the vanadyl moieties) and the qubit-linking system (the catecholate-based ligand) have played a crucial role here in preserving the long spin coherence. It should be also highlighted that coherence times are retained almost unchanged up to 100 K, a temperature which is an order of magnitude larger than that at which T_ms are reported for state-of-the-art molecular quantum gate systems.[21,23] The possibility to perform coherent spin manipulations in this system is also demonstrated by nutation experiments, performed at different microwave powers, up to 80 K at both X- and Q-bands (Fig. S7 and S8†).

The temperature dependence of T_1 for **1** shows values that perfectly match those of the single-vanadyl-qubit reference system **2** for $T > 30$ K, thus suggesting that T_1 in that temperature regime is mainly determined by structural parameters that are in common for the two systems, *i.e.* the first coordination sphere. For $T < 30$ K, the values of T_1 for the two complexes show a divergence, being shorter for **1** than for **2**. This behaviour can be related to a prevalent direct mechanism of relaxation for **1**, rather than a Raman one that seems instead dominating for **2**. Longer T_1 at low temperatures for molecules with a smaller mass but the same magnetic core has been already observed in a recent comparative study of vanadyl catecholate derivatives and tentatively attributed to the higher energy of low frequency vibrational modes admixed to rigid rotations.[39]

Frequency dependent AC susceptibility measurements were performed on a concentrated sample of **1** as a function of both temperature and applied static magnetic field (Fig. S9 and S10†). As expected for $S = 1/2$ spin systems, slow relaxation is detected only under applied magnetic fields. The extracted relaxation times (τ) show a behaviour that is qualitatively similar to that of **2** (see Fig. S11† for a comparison). Faster relaxation at low temperature is observed for **1**, in agreement with pulsed EPR findings.

Quantum gates

In the following, we illustrate how compound **1** can be used as an elementary unit for quantum information processing. Fig. 4a shows the lower part of the level diagram for **1** as a function of the external static magnetic field applied along the V···V axis z, while the full Zeeman diagram is available in Fig. S3.† For typical X or Q band EPR static fields, the electronic Zeeman interaction is the leading term in the Hamiltonian, while all the other terms act as perturbations. Indeed, the electronic Zeeman splitting separates the states into three groups, according to their total spin component along the direction of the field (M_S). Qubits can be encoded into 4 of the $(2I + 1)^2$ nuclear spin levels of the $M_S = -1$ subspace, in which both electrons are in their $m_s = -1/2$ state, *i.e.* $|\downarrow\downarrow\rangle$ (Fig. 4a). More specifically, the $m_I = 7/2$ and 5/2 states of each V nucleus are used to encode the logical $|0\rangle$ and $|1\rangle$ states of the qubits. The gaps between the nuclear states of the computational basis ($|00\rangle$, $|01\rangle$, $|10\rangle$ and $|11\rangle$) are mainly induced by the hyperfine interaction and fall in the radiofrequency range. As long as the switch (the coupled electronic spins) is frozen into its $M_S = -1$ subspace, the hyperfine interaction $\boldsymbol{I}\cdot\boldsymbol{A}\cdot\boldsymbol{s}$ is equivalent to a renormalization of the nuclear Zeeman term. Hence, the energy needed to rotate one of the nuclear spins does not depend on the state of the other, and the nuclear qubits can be considered effectively decoupled. Single-qubit gates can then be directly performed by means of rf pulses resonant with the $|0\rangle \rightarrow |1\rangle$ ($|m_I = 7/2\rangle \rightarrow |m_I = 5/2\rangle$) gap (Fig. 4a).§ In addition, R_z rotations can be directly implemented by exploiting 2π pulses semi-resonant with the $|m_I = 5/2\rangle \rightarrow |m_I = 3/2\rangle$ gap (see the ESI†).

Conversely, entanglement between qubits can be generated with the controlled-phase shift ($C\varphi$) two-qubit gate. The effect of this gate is to add a φ phase to the $|00\rangle$ component of the two-qubit wave-function and leave the other three components unaffected. In the following we will consider a particularly important $C\varphi$ gate obtained when $\varphi = \pi$, the CZ gate. This gate

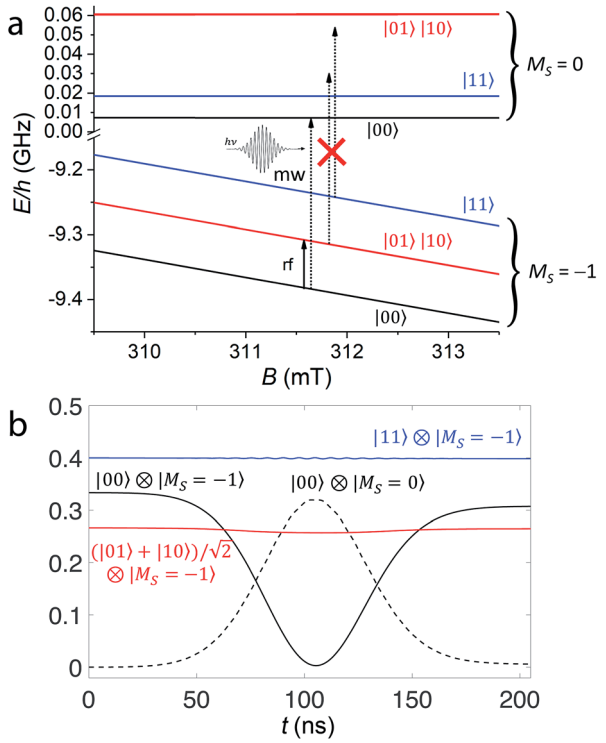

Fig. 4 (a) Zoom on the computational basis, at $B_z \approx 0.3$ mT (X-band EPR) of the energy *vs.* field diagram of the here-proposed setup based on the diagonalization of the spin Hamiltonian (1). The rf pulse needed to implement single-qubit rotations is indicated by the black solid arrow resonant with the single-qubit gap, while the dashed arrows schematically represent the implementation of a CZ gate. When a 2π micro-wave pulse resonant with the $|00\rangle|M_S = -1\rangle \rightarrow |00\rangle|M_S = 0\rangle$ transition is applied, the other components of the wave-function are unaffected by the pulse since they are off-resonant. (b) Time-evolution of the components of the two-qubit wave-function on the computational basis states under the pulse implementing a CZ gate. The system was prepared in the generic superposition of the states $\frac{1}{\sqrt{3}}|00\rangle + \sqrt{\frac{2}{15}}|01\rangle + \sqrt{\frac{2}{15}}|10\rangle + \sqrt{\frac{6}{15}}|11\rangle$ of the $M_S = -1$ subspace. We considered a static field of 0.3 mT (X-band) and a pulse of Gaussian envelope and peak amplitude 5 G.

is able to generate maximally entangled states starting from a factorized wave-function. For instance, considering $|\psi_0\rangle$ the initial factorized wave-function with both nuclear qubits in a superposition of $|0\rangle$ and $|1\rangle$ obtained by single-qubit rotations:

$$|\psi_0\rangle = \frac{|0\rangle + |1\rangle}{\sqrt{2}} \otimes \frac{|0\rangle + |1\rangle}{\sqrt{2}} = \frac{1}{2}(|00\rangle + |01\rangle + |10\rangle + |11\rangle) \quad (2)$$

The effect of a CZ gate is to implement the transformation $|\psi_0\rangle \rightarrow |\psi_1\rangle$, with

$$|\psi_1\rangle = \frac{1}{2}(-|00\rangle + |01\rangle + |10\rangle + |11\rangle) \quad (3)$$

Clearly, $|\psi_1\rangle$ cannot be written as the direct product of the separate states of the two qubits and it is a maximally entangled two-qubit state.

In the present molecular architecture, this gate can be implemented by targeting a specific EPR transition of the coupled electronic spins from the $M_S = -1$ to the corresponding $M_S = 0$ state. The hyperfine couplings make the energy required for such excitation dependent on the nuclear qubit state. Hence, applying a mw pulse resonant with the transition $|00\rangle|M_S = -1\rangle \rightarrow |00\rangle|M_S = 0\rangle$ and performing a full Rabi oscillation of the electronic spin, a π phase will be added only to the $|00\rangle$ component of the wave-function, thus implementing the CZ gate. Other components are unaffected because the corresponding transitions would occur at different frequencies, as schematically shown in Fig. 4a.

Numerical simulation

We have numerically simulated single- and two-qubit quantum gate operation through mw and rf Gaussian pulses, using the parameters determined from EPR measurements, with the same g_z and A_z for the two ions.¶ To gain more insight into the real feasibility of the gates, the effect of decoherence on the electron spin dynamics has been included by solving the master equation for the system density matrix in a Lindblad formalism[40] (see the ESI†). We have used $T_m = 1$ µs, as determined by the pulsed-EPR measurements, and neglected nuclear dephasing and relaxation, which are expected to occur on a much longer timescale. Fig. 4b shows the resulting time evolution of the components of the wave-function on the computational basis states under the 2π mw pulse required to implement the CZ gate. In order to demonstrate the possible implementation of the gate independently from the initial state, we assumed to initialize the system in a superposition $\alpha|00\rangle + \beta|01\rangle + \beta|10\rangle + \gamma|11\rangle$. Fig. 4b shows that only the $|00\rangle$ component of the system wave-function is subject to a Rabi-flop with the corresponding excited $M_S = 0$ state. The other components are practically unaffected by the pulse because they are off-resonance. This is exactly what is expected for the CZ gate. It is worth noting that the gate fidelity, *i.e.* the overlap between the ideal wave-function obtained with a perfect unitary gate and the actual result of the simulation, is high (97%) even with the inclusion of decoherence. In the present regime of parameters (with $|A_z| > |J|$), the spectral resolution needed to implement a CZ gate results from the combined effect of hyperfine and spin–spin interactions (see the ESI† for details). In particular, the closest unwanted excitation is found at about 20 MHz, thus requiring the use of a rather long pulse (about 150 ns) to ensure spectral selectivity. This means that a slightly larger spin–spin interaction, *i.e.* a shorter distance, would enable a faster processing. However, the presented results do not rely critically on the actual A_z and J values and on the precise form of the spin–spin interaction.

Quantum simulation

These promising results allow us to devise sequences of gates in order to implement quantum simulation of interesting physical models. A quantum simulator is a device that, thanks to its intrinsically quantum nature, can efficiently mimic the time evolution of other quantum systems.[47] In the present

implementation, this device would consist of the two-nuclear-qubit vanadyl-based molecular architecture, *i.e.* the physical hardware, manipulated by mw and rf pulses. Since the hardware consists of effective spin-1/2 units (the $|m_I = 7/2\rangle$, $|m_I = 5/2\rangle$ states of the two nuclear qubits in our architecture), the target Hamiltonian $\mathcal{H}$ (whose dynamics we want to simulate) needs to be encoded into a spin-1/2 model ($\tilde{\mathcal{H}}$), expressed in the following in terms of Pauli matrices, σ_α. Then, the time evolution operator induced by $\tilde{\mathcal{H}}$, $e^{-i\tilde{\mathcal{H}}t/\hbar}$, is divided into small time-steps, each implemented *via* a sequence of elementary gates (see ref. 48 and the ESI†). As a result, the physical hardware mimics the time evolution of the target, whose properties can then be extracted by the experimenter.[48–50]

As a possible proof-of-principle experiment with **1**, we propose the quantum simulation of the time evolution of the magnetization of a spin $S = 1$ experiencing quantum tunneling. The target Hamiltonian reads

$$\mathcal{H} = DS_z^2 + ES_x^2 \quad (4)$$

where D and E are the axial and transverse magnetic anisotropy parameters of the $S = 1$ system to be simulated. The spin Hamiltonian (4) can be mapped into that of two interacting spins 1/2, by considering $S = \sigma_1/2 + \sigma_2/2$.[50–52] The mapped Hamiltonian (apart from constant terms) becomes

$$\tilde{\mathcal{H}} = D\left(\frac{\sigma_{1z}}{2} + \frac{\sigma_{2z}}{2}\right)^2 + E\left(\frac{\sigma_{1x}}{2} + \frac{\sigma_{2x}}{2}\right)^2 = \frac{D}{2}\sigma_{1z}\sigma_{2z} + \frac{E}{2}\sigma_{1x}\sigma_{2x} \quad (5)$$

The corresponding time evolution operator $e^{-i\tilde{\mathcal{H}}t/\hbar} = e^{-i(D\sigma_{1z}\sigma_{2z}+E\sigma_{1x}\sigma_{2x})t/2\hbar} = e^{-iD\sigma_{1z}\sigma_{2z}t/2\hbar}e^{-iE\sigma_{1x}\sigma_{2x}t/2\hbar}$ is the product of two unitary evolutions ($e^{-iD\sigma_{1z}\sigma_{2z}t/2\hbar}$ and $e^{-iE\sigma_{1x}\sigma_{2x}t/2\hbar}$), each one corresponding to a sequence of single-qubit rotations and two-qubit Cφ gates, whose implementation is described in details in the ESI.†

Fig. 5a reports the comparison between the time evolution of the $S = 1$ magnetization calculated exactly (line) and the one simulated assuming **1** as hardware (circles), for a state initialized in $|00\rangle$. As schematically depicted in Fig. 5b, at each simulation time t three single-qubit rotations on the nuclear qubits (obtained with rf pulses) and a two-qubit $C\varphi$ gate (implemented by a 2π mw pulse) are needed to simulate the evolution.‖ For each point (red circle), corresponding to a different simulation time t, a $C\varphi$ gate with $\varphi = Et$ is implemented. Finally, the total nuclear magnetization along the static field $I_{1z} + I_{2z}$ is measured. Oscillations are reported as a function of the dimensionless parameter Et, since they occur on a timescale $2\pi/E$. In our encoding there is a direct relationship between the magnetization S_z of the simulated system and the nuclear magnetization of our hardware that corresponds to $S_z = I_{1z} + I_{2z} - 6$. The output of the quantum simulation, *i.e.* the nuclear magnetization of our hardware (red circles referring to the right axis of Fig. 5a) as a function of the rescaled variable Et, well compares with the exact one (continuous line), obtained by computing the time evolution of S_z induced by (4).

The simulation was performed assuming a static field of 3.5 T, corresponding to an electronic resonance frequency of *ca.* 98 GHz (*i.e.* W-band EPR), since this improves the gate fidelity. The latter is important when several gates are concatenated. It must also be noted that at experimentally achievable temperatures for standard spectrometers (a few K) all the computational basis states are nearly equally populated, but initialization in a pure state ($|00\rangle$) could be achieved by electron-nuclear polarization transfer[53] or heat-bath cooling techniques[36] as explained with more details in the ESI.†

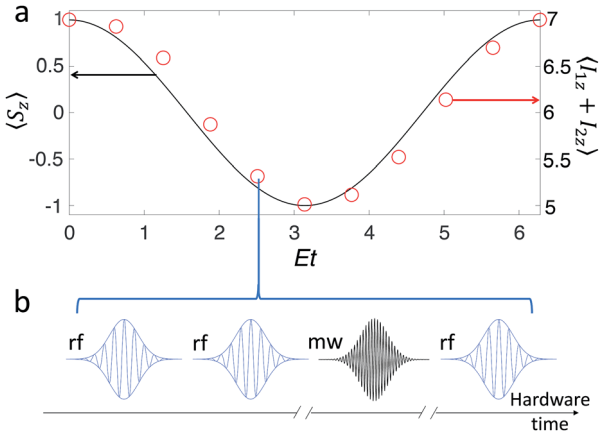

Fig. 5 (a) Digital quantum simulation of the oscillation of the magnetization of an $S = 1$ spin experiencing quantum tunneling [target Hamiltonian (4)]. The simulation was performed in a static field of 3.5 T, with the inclusion of pure dephasing effects induced by the measured $T_m = 1$ μs. The average fidelity of the sequence of gates is remarkably high (98%), as witnessed by the good agreement between exact (continuous black line, left scale) and simulated (red circles, right scale) evolution. (b) Sequence of three rf (single-qubit rotations) and one mw (two-qubit gates) pulses required to simulate each point in panel (a).

It is worth noting that our scheme is intrinsically robust against the electronic T_m. Indeed, the final average fidelity is very high (98%), even if the total time required for the simulation is 10–20 μs, much longer than T_m. In fact, the dephasing induced by the finite value of T_m affects the dynamics only during the implementation of fast (≤150 ns) two-qubit gates. Conversely, during slow single-qubit rotations (each lasting a few μs) the electronic part of the wave-function is factorized from the computational (nuclear) subspace, and hence does not affect its dynamics.

Comparing our prototypical simulator with a recent proposal also based on nuclear qubits and electronic spins,[25] we note that a much simpler gate sequence, consisting of a fast two-qubit $C\varphi$ gate and a single-qubit rotation of the nuclei, is herein required in the simulation of the elementary using interaction (first term in eqn (5)) between nuclear qubits.

Conclusions

In conclusion, through a rational design that has started from the selection of single-qubit building blocks with long coherence times we have here realized a molecular platform to implement a new quantum simulation scheme. The proposal presented herein has several remarkable advantages to be highlighted: (i) at variance with purely electron spin-based

schemes, qubits are isolated from environmental decoherence for most of the computational time; (ii) as opposite to typical NMR schemes, the interaction between pairs of qubits is not permanent, but can be rapidly switched on and off by uniform EPR pulses. This avoids unwanted two-qubit evolutions and simplifies sequences of pulses needed for quantum simulation; (iii) additional nuclear levels, that are not used to encode the qubits, can be exploited as additional resources for complex gate operations.[54,55]

The necessary experimental set-up to implement such a computational scheme requires both mw and rf excitations, although it differs from ENDOR spectrometers in the detection mode, based here on the nuclear spins.

The operation of the platform as a quantum simulator would also benefit from some chemical improvements that appear within reach. First, the dilution in a solid diamagnetic matrix would allow an efficient addressing of the individual transitions. We have previously employed low-spin Mo^{IV} = O complexes as diamagnetic analogues of V^{IV} = O systems whose stabilization will require a chemical modification of the catecholate ligands to dithiolene ones. An increase in the interaction between spin centers, reducing the length of the spacer, will also allow a better resolution of the individual electronic resonances exploitable in the computational scheme.

The present results highlight the great potential of molecular/coordination chemistry to provide a valuable contribution to quantum information technologies based on electronic and nuclear spins thanks to the intrinsic scalability of molecular architectures. We can indeed foresee further extensions of this approach to build more complex platforms, *e.g.* trimers or polynuclear assemblies, or even organize the molecular units in extended networks.

It is also clear from this study that synthetic efforts need to be accompanied by a theoretical modelling of the most promising computation platforms. This needs to be realized keeping under control key parameters, such as decoherence and magnetic interactions between metal centers, through a rational choice of the single-qubit building blocks and a careful design of the resulting polynuclear molecular architectures.

Experimental

General remarks

H_4L (*N*,*N*′-bis(2,3-hydroxybenzoyl)-1,4-phenylenediamine) was synthesized by a slightly modified literature method.[41] All other reagents were purchased from Sigma-Aldrich and used as received.

Synthesis

2,3-Dimethoxybenzoyl chloride. 2,3-Dimethoxybenzoic acid (3.0 g, 16.5 mmol) was dissolved in 10 mL of $SOCl_2$, and then a few drops of DMF were added to the mixture. The resulting solution, whose color changes from yellow-orange to yellow-green upon addition of DMF, was stirred at room temperature for 4 h. 10 mL of CCl_4 were added to the mixture and the solution was stirred for 30 minutes, and then the solvents were removed under reduced pressure. 15 mL of CCl_4 were added to the residual liquid and the volatiles were removed under reduced pressure (×4 times) to eliminate all the residual $SOCl_2$. The procedure yields 3.3 g of 2,3-dimethoxybenzoyl chloride, which crystallizes upon cooling to ambient temperature. Yield: quantitative.

***N*,*N*′-Bis(2,3-dimethoxybenzoyl)-1,4-phenylenediamine.** 3.3 g of freshly prepared 2,3-dimethoxybenzoyl chloride were dissolved in 50 mL of THF and the solution was degassed and cooled to 0 °C. Triethylamine (2.8 mL) and then 1,4-phenylenediammine (0.891 g, 8.3 mmol) were added to the dimethoxybenzoyl chloride solution. The resulting mixture was stirred for 2 h at room temperature, and then the solution was filtered to remove the precipitated tetraethylammonium chloride. The precipitate was washed with CH_2Cl_2 to solubilize part of the precipitated product, and the organic phases were evaporated under reduced pressure. The residue was dissolved in 150 mL of CH_2Cl_2 and washed with 100 mL aqueous solution of $NaHCO_3$ (0.1 M), which was back extracted with CH_2Cl_2 (2 × 50 mL). The combined organic phases were dried over $NaSO_4$ and the solvent was evaporated to yield 2.7 g of *N*,*N*′-bis(2,3-dimethoxybenzoyl)-1,4-phenylene-diamine as a white powder. Yield: 75%. ^{1}H NMR (400 MHz, $CDCl_3$): δ 10.02 (s, 2H, N*H*), 7.80 (dd, J = 8.0 Hz, J' = 1.6 Hz, 2H, Ar*H*), 7.70 (s, 4H, Ar*H*), 7.21 (dd, J = 8.0 Hz, J' = 8.0 Hz, 2H, Ar*H*), 7.10 (dd, J = 8.0 Hz, J' = 1.5 Hz, 2H, Ar*H*), 4.00 (s, 6H, OCH_3), 3.94 (s, 6H, OCH_3).

***N*,*N*′-Bis(2,3-dihydroxybenzoyl)-1,4-phenylenediamine.** 2.7 g (6.2 mmol) of *N*,*N*′-bis(2,3-dimethoxybenzoyl)-1,4-phenylenediamine were dissolved in 150 mL of CH_2Cl_2 and the solution was cooled to 0 °C. 30 mL of a 1.0 M CH_2Cl_2 solution of BBr_3 were added to the resulting mixture with the immediate formation of a white precipitate. The mixture was stirred overnight, and then the solvent was evaporated under reduced pressure. To the residual solid water (50 mL) was added and the mixture was stirred at 90 °C for 1 h. The precipitate of *N*,*N*′-bis(2,3-dihydroxybenzoyl)-1,4-phenylenediamine was separated from the solution by vacuum filtration and washed several times with water, and then dried under vacuum over P_2O_5. Yield: quantitative. ^{1}H NMR (400 MHz, DMSO-d_6): δ 11.74 (bs, 2H, O*H*), 10.38 (s, 2H, N*H*), 9.48 (bs, 2H, O*H*), 7.68 (s, 4H, Ar*H*), 7.44 (dd, J = 8.1 Hz, J' = 1.2 Hz, 2H, Ar*H*), 6.98 (dd, J = 8.1 Hz, J' = 1.2 Hz, 2H, Ar*H*), 6.77 (dd, J = 8.1 Hz, J' = 8.1 Hz, 2H, Ar*H*).

$[Ph_4P]_4[(VO)_2(L)_2]$ (1). A water solution (10 mL) of $VOSO_4 \cdot xH_2O$ (180 mg, 0.95 mmol) was added dropwise to a water solution (15 mL) of *N*,*N*′-Bis(2,3-dihydroxybenzoyl)-1,4-phenylene-diamine (300 mg, 0.79 mmol) deprotonated with NaOH (126 mg, 3.2 mmol). The solution was stirred at room temperature for 2 h, and then a methanol solution (5 mL) of Ph_4PBr (500 mg, 1.2 mmol) was added, inducing the immediate precipitation of complex **1** as a green-blue solid. The solid was filtered and washed several times with hot water, and then dried under vacuum over P_2O_5. Yield: 72%. Elemental anal. calcd for $C_{136}H_{104}N_4O_{14}P_4V_2$: C, 72.79; H, 4.67; N, 2.50. Found: C, 72.02; H, 4.51; N, 2.38. FT-IR ($\tilde{\nu}_{max}$/cm^{-1}, KBr pellet): 3077vw, 3055w, 3023vw, 2994vw, 1644s, 1604w, 1585m, 1548w, 1513vs, 1483w, 1463m, 1456vs, 1405w, 1340w, 1309m, 1287w, 1251s, 1207s,

1164w, 1108s, 1058w, 995w, 960m, 930m, 839w, 787vw, 748m, 722s, 670s, 641m, 526vs, 472w. ESI-MS, *m*/*z* found (calcd): (negative ion mode) 521.21 (521.24) $[Na_4[(VO)_2(L)_2]\cdot CH_3OH]^{2-}$; 955.51 (955.52) $[Na_3[(VO)_2(L)_2]]^-$; (positive ion mode) 339.40 (339.39) $[Ph_4P^+]$.

Characterization

^{1}H NMR spectra were measured at 298 K on a Bruker Ultrashield Plus 400 MHz spectrometer. C, H, and N analyses were performed with a CHN–S Flash E1112 Thermo Finnigan analyzer. FT-IR spectra were obtained on KBr pellets and collected with a Shimadzu-8400S spectrophotometer. Electrospray Ionization Mass Spectrometry (ESI-MS) data were acquired on HPLC grade methanol by using a Thermo Scientific LCQ-Fleet mass spectrometer under electrospray ionization (Thermo Scientific, Austin TX, USA) by direct infusion with a 500 KL Hamilton microsyringe. Data were acquired over hundred scans after the stabilization of the ionic current for 5 min at a sample flow of 10 μl min^{-1}. The mass spectrometer parameters used were: sheet gas flow = 10, auxiliary gas flow = 0, sweep gas flow = 0, spray voltage = 5.00 kV, capillary tube temperature = 220 °C, and capillary voltage = 12.0 V.

Electron paramagnetic resonance

CW X-Band EPR spectra were recorded on a Bruker Elexsys E500 spectrometer equipped with a SHQ cavity ($\nu = 9.39$ GHz). Low temperature measurements were obtained using an Oxford Instruments ESR900 continuous flow helium cryostat. Pulsed EPR measurements were carried out with a Bruker Elexsys E580 at X-band ($\nu \cong 9.70$ GHz) equipped with a flexline dielectric ring ENDOR resonator (Bruker EN 4118X-MD4). Temperatures between 4.5 and 100 K were obtained with an Oxford Instruments CF935 continuous flow helium cryostat. Echo detected field swept EPR spectra were recorded by using the Hahn Echo pulse sequence ($\pi/2 - \tau - \pi - \tau -$ echo) with a fixed interpulse delay time $\tau = 200$ ns, $t_{\pi/2} = 16$ ns and $t_\pi = 32$ ns. Both phase memory times were measured by using the Hahn Echo sequence upon increasing the interpulse delay τ starting from $\tau = 98$ ns. Spin-lattice relaxation times were measured using the standard inversion recovery sequence ($\pi - t_d - \pi/2 - \tau - \pi - \tau -$ echo), with $\pi/2 = 16$ ns. The uncertainty in T_1 estimated from replicate measurements was 5–10% depending upon the signal-to-noise ratio at a given temperature-field combination.

HYSCORE spectroscopy

Six-pulse Hyperfine Sublevel Correlation experiments[56,57] were carried out with the extended pulse sequence $(\pi/2)_x - \tau_1 - (\pi)_x - \tau_1 - (\pi/2)_y - t_1 - (\pi)_y - t_2 - (\pi/2)_y - \tau_2 - (\pi)_y - \tau_2 -$ echo. An eight-step phase cycle was adopted in order to eliminate unwanted echoes. The t_1 and t_2 time intervals were incremented in steps of 16 ns, starting from 100 ns to 3300 ns. Pulse lengths $t_{\pi/2} = 16$ ns and $t_\pi = 32$ ns, a 0.5 kHz shot repetition rate, and $\tau_1 = \tau_2 = 110$ ns were used. The time traces of the HYSCORE spectra were baseline corrected with a third-order polynomial, apodized with a Hamming window, and zero-filled. After two-dimensional Fourier transformation, the absolute-value spectra were calculated.

DC and AC magnetic characterization

The DC (direct current) magnetic susceptibility measurements were performed with a Quantum Design Magnetic Property Measurement System (MPMS) SQUID magnetometer. The measurements were performed on a polycrystalline sample of **1** (4.3 mg) in the 2.0–300 K T range by applying a static magnetic field of 1.0 T for $T > 20$ K and 0.1 T for $T < 20$ K. AC susceptibility measurements were performed at $T = 5$ K with applied magnetic fields up to 8.5 T on a polycrystalline sample of compound **1** (49.4 mg) by using a Quantum Design Physical Property Measurement System (PPMS) equipped with a AC susceptometer operating in the 10 Hz to 10 kHz frequency range. Data were corrected for the sample holder previously measured using the same conditions and for the diamagnetic contributions as deduced by using Pascal's constant tables.[58]

Conflicts of interest

There are no conflicts to declare.

Acknowledgements

Italian MIUR, through the PRIN project QCNaMoS (2015-HYFSRT), and Fondazione Ente Cassa di Risparmio di Firenze are acknowledged for financial support. European COST Action CA15128 MOLSPIN is also acknowledged. We are indebted to Dr Marie-Emmanuelle Boulon (University of Florence) for her assistance in CW-EPR data collection and to Mr Lorenzo Tesi (University of Florence) for stimulating discussions.

Notes and references

‡ We neglected here the isotropic part of the dipolar interactions, since this is calculated to be negligible in the point dipole approximation when considering the estimated distance between the V=O centers and the measured anisotropy of g.

§ Notice that the $|0\rangle \rightarrow |1\rangle$ ($|m_I = 7/2\rangle \rightarrow |m_I = 5/2\rangle$) transition is made distinguishable from other $|m_I\rangle \rightarrow |m_I \pm 1\rangle$ transitions by second order shifts due to virtual hyperfine-induced excitations, as well as by nuclear quadrupole coupling PI_z^2 typical of penta-coordinated vanadyl ions (*ca.* −0.9 MHz).[33] It is worth stressing that the precise value of P does not affect the feasibility of the proposed quantum gates.

¶ We need $J \gg \Delta g_z \mu_B B$, $\Delta A_z m_I$ to induce a collective excitation of the two electronic spins.

‖ For the system initialized in $|00\rangle$, gates corresponding to the evolution $e^{-iD\sigma_{1z}\sigma_{2z}t/2\hbar}$ do not affect the dynamics.

1 M. Nielsen and I. Chuang, *Quantum Computation and Quantum Information*, Cambridge University Press, 2004.
2 D. P. DiVincenzo, *Science*, 1995, **270**, 255–261.
3 T. D. Ladd, F. Jelezko, R. Laflamme, Y. Nakamura, C. Monroe and J. L. O'Brien, *Nature*, 2010, **464**, 45–53.
4 J. Clarke and F. K. Wilhelm, *Nature*, 2008, **453**, 1031–1042.
5 S. Carretta, A. Chiesa, F. Troiani, D. Gerace, G. Amoretti and P. Santini, *Phys. Rev. Lett.*, 2013, **111**, 110501.

6 E. Knill, R. Laflamme and G. J. A. Milburn, *Nature*, 2001, **409**, 46–52.
7 B. Hacker, S. Welte, G. Rempe and S. A. Ritter, *Nature*, 2016, **536**, 193–196.
8 G. Tosi, F. A. Mohiyaddin, V. Schmitt, S. Tenberg, R. Rahman, G. Klimeck and A. Morello, *Nat. Commun.*, 2017, **8**, 450.
9 B. Pingault, J. N. Becker, C. H. H. Schulte, C. Arend, C. Hepp, T. Godde, A. I. Tartakovskii, M. Markham, C. Becher and M. Atatüre, *Phys. Rev. Lett.*, 2014, **113**, 263601.
10 K. Bader, D. Dengler, S. Lenz, B. Endeward, S.-D. Jiang, P. Neugebauer and J. van Slageren, *Nat. Commun.*, 2014, **5**, 5304.
11 K. Bader, M. Winkler and J. van Slageren, *Chem. Commun.*, 2016, **52**, 3623–3626.
12 M. Atzori, E. Morra, L. Tesi, A. Albino, M. Chiesa, L. Sorace and R. Sessoli, *J. Am. Chem. Soc.*, 2016, **138**, 11234–11244.
13 M. Atzori, L. Tesi, E. Morra, M. Chiesa, L. Sorace and R. Sessoli, *J. Am. Chem. Soc.*, 2016, **138**, 2154–2157.
14 L. Tesi, E. Lucaccini, I. Cimatti, M. Perfetti, M. Mannini, M. Atzori, E. Morra, M. Chiesa, A. Caneschi, L. Sorace and R. Sessoli, *Chem. Sci.*, 2015, **7**, 2074–2083.
15 C.-J. Yu, M. J. Graham, J. M. Zadrozny, J. Niklas, M. D. Krzyaniak, M. R. Wasielewski, O. G. Poluektov and D. E. Freedman, *J. Am. Chem. Soc.*, 2016, **138**, 14678–14685.
16 J. M. Zadrozny, J. Niklas, O. G. Poluektov and D. E. Freedman, *ACS Cent. Sci.*, 2015, **1**, 488–492.
17 C. J. Wedge, G. A. Timco, E. T. Spielberg, R. E. George, F. Tuna, S. Rigby, E. J. L. McInnes, R. E. P. Winpenny, S. J. Blundell and A. Ardavan, *Phys. Rev. Lett.*, 2012, **108**, 107204.
18 G. A. Timco, E. J. L. McInnes and R. E. P. Winpenny, *Chem. Soc. Rev.*, 2013, **42**, 1796–1806.
19 A. Chiesa, G. F. S. Whitehead, S. Carretta, L. Carthy, G. A. Timco, S. J. Teat, G. Amoretti, E. Pavarini, R. E. P. Winpenny and P. Santini, *Sci. Rep.*, 2014, **4**, 7423.
20 A. Ardavan, A. M. Bowen, A. Fernandez, A. J. Fielding, D. Kaminski, F. Moro, C. A. Muryn, M. D. Wise, A. Ruggi, E. J. L. McInnes, K. Severin, G. A. Timco, C. R. Timmel, F. Tuna, G. F. S. Whitehead and R. E. P. Winpenny, *Npj Quantum Inf.*, 2015, **1**, 15012.
21 J. Ferrando-Soria, E. Moreno Pineda, A. Chiesa, A. Fernandez, S. A. Magee, S. Carretta, P. Santini, I. J. Vitorica-Yrezabal, F. Tuna, G. A. Timco, E. J. L. McInnes and R. E. P. Winpenny, *Nat. Commun.*, 2016, **7**, 11377.
22 F. Luis, A. Repollés, M. J. Martínez-Pérez, D. Aguilà, O. Roubeau, D. Zueco, P. J. Alonso, M. Evangelisti, A. Camón, A. J. Sesé, L. A. Barrios and G. Aromí, *Phys. Rev. Lett.*, 2011, **107**, 117203.
23 D. Aguila, L. A. Barrios, V. Velasco, O. Roubeau, A. Repolles, P. J. Alonso, J. Sese, S. J. Teat, F. Luis and G. Aromi, *J. Am. Chem. Soc.*, 2014, **136**, 14215–14222.
24 S. Nakazawa, S. Nishida, T. Ise, T. Yoshino, N. Mori, R. D. Rahimi, K. Sato, Y. Morita, K. Toyota, D. Shiomi, M. Kitagawa, H. Hara, P. Carl, P. Höfer and T. Takui, *Angew. Chem., Int. Ed.*, 2012, **51**, 9860–9864.
25 S. Yamamoto, S. Nakazawa, K. Sugisaki, K. Sato, K. Toyota, D. Shiomi and T. Takui, *Phys. Chem. Chem. Phys.*, 2015, **17**, 2742–2749.
26 J. A. Jones, *Prog. Nucl. Magn. Reson. Spectrosc.*, 2011, **59**, 91–120.
27 C. Godfrin, A. Ferhat, R. Ballou, S. Klyatskaya, M. Ruben, W. Wernsdorfer and F. Balestro, *Phys. Rev. Lett.*, 2017, **119**, 187702.
28 E. Moreno-Pineda, C. Godfrin, F. Balestro, W. Wernsdorfer and M. Ruben, *Chem. Soc. Rev.*, 2018, **47**, 501.
29 J. J. L. Morton, A. M. Tyryshkin, A. Ardavan, S. C. Benjamin, K. Porfyrakis, S. A. Lyon and G. A. D. Briggs, *Nat. Phys.*, 2005, **2**, 40.
30 Y. Zhang, C. A. Ryan, R. Laflamme and J. Baugh, *Phys. Rev. Lett.*, 2011, **107**, 170503.
31 K. Sato, S. Nakazawa, R. Rahimi, T. Ise, S. Nishida, T. Yoshino, N. Mori, K. Toyota, D. Shiomi, Y. Yakiyama, Y. Morita, M. Kitagawa, K. Nakasuji, M. Nakahara, H. Hara, P. Carl, P. Hofer and T. Takui, *J. Mater. Chem.*, 2009, **19**, 3739–3754.
32 R. R. Darabad, K. Sato, P. Carl, P. Höfer, R. Laflamme and T. Takui in *Electron Spin Resonance (Esr) Based Quantum Computing*, ed. T. Takui, L. Berliner and G. Hanson, Springer New York, New York, NY, 2016, pp. 25–50.
33 J. J. Pla, K. Y. Tan, J. P. Dehollain, W. H. Lim, J. J. L. Morton, F. A. Zwanenburg, D. N. Jamieson, A. S. Dzurak and A. Morello, *Nature*, 2013, **496**, 334.
34 M. Mehring and J. Mende, *Phys. Rev. A*, 2006, **73**, 052303.
35 J. S. Hodges, J. C. Yang, C. Ramanathan and D. G. Cory, *Phys. Rev. A*, 2008, **78**, 010303.
36 M. Mehring, J. Mende and W. Scherer, *Phys. Rev. Lett.*, 2003, **90**, 153001.
37 D. K. Park, G. Feng, R. Rahimi, S. Labruyère, T. Shibata, S. Nakazawa, K. Sato, T. Takui, R. Laflamme and J. Baugh, *Quantum Inf. Process.*, 2015, **14**, 2435–2461.
38 J. Zhang, D. Burgarth, R. Laflamme and D. Suter, *Phys. Rev. A*, 2015, **91**, 012330.
39 M. Atzori, S. Benci, E. Morra, L. Tesi, M. Chiesa, R. Torre, L. Sorace and R. Sessoli, *Inorg. Chem.*, 2018, **57**, 731.
40 H.-P. Breuer and F. Petruccione, *The Theory of Open Quantum Systems*, Oxford University Press, 2002.
41 M. J. Graham, C.-J. Yu, M. D. Krzyaniak, M. R. Wasielewski and D. E. Freedman, *J. Am. Chem. Soc.*, 2017, **139**, 3196–3201.
42 B. Kersting, M. Meyer, R. E. Powers and K. N. Raymond, *J. Am. Chem. Soc.*, 1996, **118**, 7221–7222.
43 M. Meyer, B. Kersting, R. E. Powers and K. N. Raymond, *Inorg. Chem.*, 1997, **36**, 5179–5191.
44 C. V. Grant, J. A. Ball, B. J. Hamstra, V. L. Pecoraro and R. D. Britt, *J. Phys. Chem. B*, 1998, **102**, 8145–8150.
45 B. Kirste and H. Van Willigen, *J. Phys. Chem.*, 1982, **86**, 2743–2749.
46 S. Stoll and A. Schweiger, *J. Magn. Reson.*, 2006, **178**, 42–55.
47 R. P. Feynman, *Int. J. Theor. Phys.*, 1982, **21**, 467–488.
48 S. Lloyd, *Science*, 1996, **273**, 1073–1078.
49 I. Buluta and F. Nori, *Science*, 2009, **326**, 108–111.
50 I. M. Georgescu, S. Ashhab and F. Nori, *Rev. Mod. Phys.*, 2014, **86**, 153–185.

51 P. Santini, S. Carretta, F. Troiani and G. Amoretti, *Phys. Rev. Lett.*, 2011, **107**, 230502.
52 A. Chiesa, P. Santini, D. Gerace, J. Raftery, A. A. Houck and S. Carretta, *Sci. Rep.*, 2015, **5**, 16036.
53 C. Tanmoy, Z. Jingfu and S. Dieter, *New J. Phys.*, 2017, **19**, 073030.
54 M. D. Jenkins, Y. Duan, B. Diosdado, J. J. García-Ripoll, A. Gaita-Arino, A. C. Giménez-Saiz, P. J. Alonso, E. Coronado and F. Luis, *Phys. Rev. B*, 2017, **95**, 064423.
55 B. P. Lanyon, M. Barbieri, M. P. Almeida, T. Jennewein, T. C. Ralph, K. J. Resch, G. J. Pryde, J. L. O'Brien, A. Gilchrist and A. G. White, *Nat. Phys.*, 2008, **5**, 134–140.
56 R. Song, Y. C. Zhong, C. J. Noble, J. R. Pilbrow and D. R. Hutton, *Chem. Phys. Lett.*, 1995, **237**, 86–90.
57 B. Kasumaj and S. Stoll, *J. Magn. Reson.*, 2008, **190**, 233–247.
58 G. A. Bain and J. F. Berry, *J. Chem. Educ.*, 2008, **85**, 532.